Ground- and ship-based microwave radiometer measurements during EUREC4A

Sabrina Schnitt[1], Andreas Foth[2], Heike Kalesse-Los[2], Mario Mech[1], Claudia Acquistapace[1], Friedhelm Jansen[3], Ulrich Löhnert[1], Bernhard Pospichal[1], Johannes Röttenbacher[2], Susanne Crewell[1], and Bjorn Stevens[3]

[1]Institute for Geophysics and Meteorology, University of Cologne, Cologne, Germany
[2]Leipzig Institute for Meteorology (LIM), Leipzig University, Leipzig, Germany
[3]Max Planck Institute for Meteorology, Hamburg, Germany

Correspondence: Sabrina Schnitt (s.schnitt@uni-koeln.de)

Abstract.

During the EUREC[4]A field study, microwave radiometric measurements were performed at Barbados Cloud Observatory (BCO) and aboard the RV Meteor and RV Maria S Merian. We present retrieved Integrated Water Vapor (IWV), Liquid Water Path (LWP) and temperature and humidity profiles as a unified, quality-controlled, multi-site dataset on a three second temporal
5   resolution for a core period between January 19, 2020 and February 14, 2020 in which all instruments were operational. 14-channel K- and V-band measurements were performed at BCO and aboard the RV Meteor, and combined radar-radiometer measurements of a W-band Doppler radar with a single-channel radiometer instrument were conducted at $89\,\mathrm{GHz}$ onboard the RV Meteor and RV Maria S Merian. Mean IWV of $31.8\,\mathrm{kg\,m^{-2}}$ matches independent radiosoundings at BCO with a root-mean-square difference of $1.1\,\mathrm{kg\,m^{-2}}$. Mean LWP conditions in confident cloudy, non-precipitating conditions ranged between
10   $66.5\,\mathrm{g\,m^{-2}}$ at BCO to $40.4\,\mathrm{g\,m^{-2}}$ aboard the RV Maria S Merian. Aboard the ships, $90\,\%$ of LWP was below $120\,\mathrm{g\,m^{-2}}$ with an uncertainty of $30\,\%$ at LWP of $50\,\mathrm{g\,m^{-2}}$. Up to $30\,\%$ of confident cloudy profiles ranged below the LWP detection limit due to optically thin clouds.

The data set comprises of processed raw-data (Level 1), full quality-controlled post-processed instrument data (Level 2), a unified temporal resolution (Level 3), and a ready-to-use multi-site time series of IWV and LWP (Level 4), available to the pub-
15   lic via AERIS (https://doi.org/10.25326/454, Schnitt et al., 2023). The data set complements the airborne LWP measurements conducted during EUREC[4]A and provides a benchmark tool for model-observation studies.

1   Introduction

The subtropical oceans are ubiquitously covered by shallow trade-wind cumulus clouds. While small in individual size and height, cloud fields are large in their extent, which makes them important for the radiative budget through the short-wave
20   reflected radiation which is directly related to the liquid water amount and distribution in the cloud. Large inter-model spreads of climate sensitivity are thought to be related to the representation of these clouds in current climate models (Bony et al., 2015; Dufresne and Bony, 2008; Vial et al., 2013; Zelinka et al., 2020; Jahangir et al., 2021) and their potential role in mediating

the long-wave radiative response to warming (Stevens and Kluft, 2023). Open questions include the interaction of these clouds with their environment, and their coupling to circulation and convection (Bony et al., 2017). In order to elucidate the underlying

25 processes of the interactions, high quality and fine resolution observations were gathered during the EUREC⁴A field study in January and February 2020 (Stevens et al., 2021) over the Tropical Atlantic windward and in the close vicinity of Barbados. A range of complementary measurements were performed by four different research aircraft (Konow et al., 2021; Bony et al., 2022; Pincus et al., 2021), and by ground- and ship-based observations (e.g. Acquistapace et al., 2022; Kalesse-Los et al., 2023). Microwave radiometric measurements were conducted at Barbados Cloud Observatory (BCO, Stevens et al., 2016),

30 as well as aboard the RV Meteor (later referred to as Meteor) and the RV Maria S Merian (referred to as Merian). Here, we present the data set of Integrated Water Vapor (IWV), Liquid Water Path (LWP) as well as profiles of temperature T and absolute humidity ρ_v retrieved from the measurements at BCO, and aboard the Meteor and Merian.

Passive microwave radiometry is widely in use from satellite, airborne platforms such as the High Altitude LOng range (HALO) aircraft (Mech et al., 2014; Stevens et al., 2019), research vessels like the RV Polarstern (Walbröl et al., 2022),

35 and ground-based supersites like the Atmospheric Radiation Measurement (ARM) program (Stokes and Schwartz, 1994) or CloudNet (Illingworth et al., 2007). In EUREC⁴A's area of study, LWP conditions have been previously measured from HALO during the Next Generation Aircraft Remote Sensing for Validation Studies (NARVAL) I and II campaigns in different seasons (Stevens et al., 2019; Jacob et al., 2019; Schnitt et al., 2017). A multi-decade climatology of LWP is available from satellite observations at a horizontal resolution of $0.25°$ (Elsaesser et al., 2017). During EUREC⁴A, airborne measurements were again

40 performed by the HALO microwave package HAMP (HAMP, Mech et al., 2014), as described in Konow et al. (2021) and available in Jacob (2021).

As opposed to remote sensing in the visible or infrared parts of the spectrum, passive microwave radiometer (MWR) measurements are sensitive to the full vertical column as clouds are semi-transparent in the microwave frequencies. Water vapor, oxygen, and liquid water emit at characteristic frequencies. Emissions can be measured as brightness temperatures T_B follow-

45 ing Planck's law. While water vapor and oxygen emit in absorption bands in the K- and V-band and F- and G-band, respectively, liquid water emissions increase with increasing frequency (Ulaby, 2014). Therefore, channels in the K-band around the 22.24 GHz line need to be paired with measurements from a window channel at 31.4 GHz or 90 GHz to allow simultaneous the retrieval of IWV and LWP (Westwater, 1978; Löhnert and Crewell, 2003). Absolute humidity profiles with limited vertical resolution (Löhnert et al., 2009) can be derived if multiple channels are located along the wing of the 22.24 or 183 GHz

50 line. Temperature profiles of better than 500 m vertical resolution can be obtained from the oxygen absorption complex around 50 GHz. A higher resolution can be achieved by scanning at different elevation angles (Crewell and Lohnert, 2007). A scattering contribution to the measured T_B only occurs if ice is present in clouds for frequencies above 90 GHz.

The Humidity and Temperature PROfiler HATPRO (Rose et al., 2005) is equipped with seven channels in the K-band and seven channels in the V-band. Measurements can be obtained in non-precipitating conditions as a wet radome causes

55 non-atmospheric liquid emissions. The instruments are equipped with a blowing unit to mitigate the deposition of rain on the radomes during and after precipitation events. Retrieval methods based on statistical regression techniques (Löhnert and Crewell, 2003) or neural networks (Cadeddu et al., 2009; Jacob et al., 2019) are applied to the T_B measurements to retrieve

Table 1. Overview of passive microwave measurements performed during EUREC[4]A at BCO, aboard the Meteor and the Merian. Measured quantities, retrieved variables, each instrument's scan strategy as well as the covered time periods are given.

	BCO	Meteor		Merian
instrument	**BCOHAT** (Rose et al., 2005)	**LIMHAT**	**LIMRAD** (Kalesse-Los et al., 2023)	**MSMRAD** (Acquistapace et al., 2022)
T_B measured at	22.24 - 31.4 GHz (7 channels) 51 - 58 GHz (7 channels)	same as BCOHAT	89.0	89.0
retrieved quantities	IWV, LWP precipitation mask T, ρ_v profiles	IWV, LWP precipitation mask T, ρ_v profiles	clear-sky IWV, LWP precipitation mask	clear-sky IWV, LWP precipitation mask
scan strategy	zenith elevation scan every 15 min	zenith unstabilized elevation scan full hour	zenith, stabilized	zenith, stabilized
time coverage	January 01 - February 14, 2020	January 15 - February 19, 2020	January 17 - February 19, 2020	January 16 - February 19, 2020

IWV, LWP and thermodynamic profiles. A HATPRO is permanently installed at BCO (Stevens et al., 2016), here referred to as BCOHAT. During EUREC[4]A, BCOHAT measurements were complemented by HATPRO measurements aboard the Meteor performed by the Leipzig Institute for Meteorology (LIM), here referred to as LIMHAT. Aboard the Meteor, a 94 GHz cloud radar (Küchler et al., 2017) was installed, equipped with a passive radiometer channel measuring T_B at 89 GHz (Kalesse-Los et al., 2023), here referred to as LIMRAD. A similar instrument was stationed aboard the Merian (Acquistapace et al., 2022), here referred to as MSMRAD. These single-channel measurements are suitable to retrieve IWV in cloud-free conditions, and LWP in cloudy conditions if IWV is known, e.g. through radiosoundings or re-analysis.

This paper describes the network of continuous ground- and ship-based microwave radiometer measurements in a core period of January 19, 2020, until February 14, 2020, during which all four instruments were operational. We document setup and installation of the instruments (Sec 2), introduce retrieval methods (Sec 3) and data processing (Sec 4), and evaluate retrieved IWV (Sec 5), LWP (Sec 6), as well as temperature and humidity profiles (Sec 7). We conclude the paper (Sec 8) by summarizing and highlighting further scientific applications for this data set.

2 MWR network

During EUREC[4]A, passive radiometer measurements were performed from BCO, the Meteor, and the Merian. The following subsections describe the installation details of the instruments at each site, respectively. Instruments' details and retrieved quantities are summarized in Tab 1. Installation is shown in Fig 1. Microwave radiometer measurements were not performed aboard the RV Ronald H Brown.
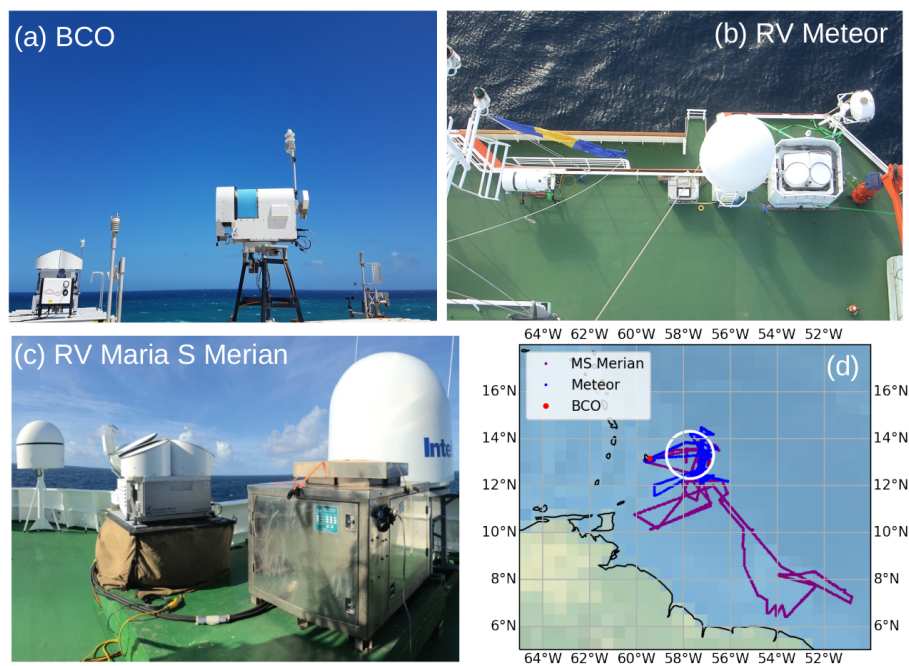
Figure 1. Installation of (a) MWR BCOHAT at BCO, (b) MWR LIMHAT and cloud radar LIMRAD aboard the Meteor, (c) cloud radar MSMRAD aboard the Merian, and (d) map of operations with BCO (red), and Meteor (blue) and Merian (purple) ship tracks, including the circle flown by the HALO aircraft (white) for orientation.

2.1 BCO

The RPG-HATPRO Generation 5 multi-channel microwave radiometer BCOHAT is continuously installed on top of a container at 25m asl in proximity to the island shore (see Fig 1(a) and Stevens et al., 2016). An absolute calibration with liquid nitrogen was performed before the start of the EUREC⁴A operations on January 14, 2020. BCOHAT measured according to the following regularly-occurring scan strategy: azimuth scans at 30° elevation angle were performed for the duration of 5 minutes every 40 minutes, followed by an elevation scan covering 11 elevation angles (90. , 30, 19.2, 14.4, 11.4, 8.4, 6.6, 5.4, 4.8, 4.2°) at 0° azimuth position (later referred to as elevation scan, Crewell and Lohnert (2007)). Zenith measurements are performed for 15 minutes at 165° azimuth (*ocean mode*) and at 267° (*island mode*), respectively, during which measurements are performed every 2 seconds. Due to technical difficulties with the scanning unit, the scanning strategy changed after February 1, 2020: azimuth scans were not performed, and zenith operation was limited to ocean mode. Elevation scans are available every 15 minutes. These technical difficulties also affected the associated BCOHAT weather station. From January 26, 2020, onwards, data from the adjacent BCO weather station was used instead to flag measurements for precipitation (https://doi.org/10.25326/54). No measurements were performed between January 29 and 31, 2020, due to maintenance on the instrument.

2.2 Meteor

90 Onboard the Meteor, the Leipzig Institute for Meteorology (LIM) of Leipzig University operated an MWR type RPG-HATPRO Generation 5 (here referred to as LIMHAT) and a radar-radiometer system of type RPG-FMCW-94 dual polarization (DP) operating actively in the W-band (94 GHz) and containing a passive radiometer channel at 89 GHz (Küchler et al., 2017; Kalesse-Los et al., 2023, here referred to as LIMRAD). Both instruments were placed 4.5m apart on the navigation deck of the ship at 15.8m above sea Level to avoid sea spray. LIMHAT operated at a temporal resolution of 1s in zenith mode. Elevation

95 scans, as done by BCOHAT, were performed by LIMHAT every full hour. An absolute calibration with liquid nitrogen was performed on January 15, 2020.

LIMRAD was operated with two different chirp programs specified in Kalesse-Los et al. (2023). Between January 17 and 29, 2020, and Jan 31 and February 28, 2020, the temporal resolution of LIMRAD was 2.9 s and 1.6 s, respectively. Radar absolute calibration was performed on January 16, 2020. Data gaps exist between January 27 and 31, 2020 when different radar chirp

100 table settings were tested, and on February 03, 2020, when all instruments had to be turned off while the Meteor was near Trinidad. As explained in Kalesse-Los et al. (2023), LIMRAD was operated in a novel passive horizontal stabilization system (two-axle cardanic mount) to assure zenith-pointing of the instrument. Stabilization is required to eliminate the effect of horizontal wind on the radar Doppler velocities. Means and standard deviations of absolute values of radar attitude measurements amounted to $0.36°+-0.31°$. It should be noted that since LIMRAD was operated in a horizontal stabilization platform while

105 LIMHAT was not, the exact (near-zenith) viewing direction of both instruments was not always the same. This effect should be negligible for retrieved IWV and LWP, however, as the larger opening angle of the LIMHAT (half-power beamwidth HPBW = $3.5°$) covered the LIMRAD column (HPBW = $0.5°$) even in events of slight mis-pointing.

Two distinct periods of measurement allow a direct comparison of the ship-based measurements. On January 19, 2020 between 00 and 12 UTC, both RVs were steaming next to one another from -58 °W to -57.3 °W between 13.8 and 13.75 °N. On

110 February 07, 2020, the ships were collocated at -57.2 °W and 12.4 °N between 11 and 18 UTC.

2.3 Merian

Aboard the Merian, the Institute for Geophysics and Meteorology of the University of Cologne operated a radar-radiometer system of the type RPG-FMCW-94 dual polarization (DP) of the same kind as LIMRAD which measures in the W-band (94 GHz) and includes a passive radiometer channel at 89 GHz (Küchler et al., 2017, here referred to as MSMRAD). The system

115 was positioned on an active stabilization platform from the US-Atmospheric Radiation Measurement (ARM) program Mobile Facility 2 which keeps the radar in zenith position by adapting the table surface position to compensate for ship motions (see Acquistapace et al., 2022, for more information). As for LIMRAD, stabilization helps eliminate the effect of horizontal wind and ship roll and pitch tilting from the radar Doppler velocities. MSMRAD was operated with three chirp programs, established after initial testing, and worked for the entire campaign. The chirp programs had 0.846, 0.786, and 1.124 s integration time,

120 respectively, resulting in brightness temperatures at 3 second temporal resolution (see Table 2 in Acquistapace et al., 2022). The data browser (https://bit.ly/3ZcAusN) displays availability and observational quality for every day of the entire campaign.

3 Retrievals

This section presents the retrieval methods applied to the HATPRO and single-channel 89 GHz measurements. IWV, LWP, temperature and humidity profiles are retrieved from HATPRO, while the single-channel measurements provide estimates for
125 LWP and clear-sky IWV.

3.1 HATPRO

IWV, LWP as well as coarse temperature and humidity profiles are retrieved using a statistical quadratic regression retrieval based on the measured T_B (see Eq. 1 with k indicating the number of channel). The seven K-band channels (22-31 GHz, channel 1-7) provide information for IWV, LWP and the absolute humidity profiles, while the seven V-band channels (51-
130 58 GHz, channels 8-14) are used for temperature profiling. The IDL software *MWR PRO* was used to process the data (https://github.com/igmk/actris_mwr_pro/blob/main/mwr_pro_idl_v04.zip).

$$\text{LWP} = c_0 + \sum_{k=0}^{N=6} c_{1,k} \cdot T_{B,k} + c_{2,k} \cdot T_{B,k}^2 \qquad (1)$$

The coefficients c_0, c_1 and c_2 are derived from a climatological training data set linking atmospheric conditions to T_B acquired from a radiative transfer model as described in Löhnert and Crewell (2003) and, more recently, in Walbröl et al.
135 (2022). Details on the used radiative transfer model can be found in Walbröl et al. (2022) and references therein. A large data set was built on 10,871 daily radiosoundings launched from 1990 until 2018 from Grantley Adams International Airport (GAIA, station ID 78954 TBPB) in close vicinity to BCO. Sounding measurements were obtained from http://weather.uwyo.edu/upperair/sounding.html. During EUREC[4]A radiosoundings of the type GRAW DFM-09 were used (Bock et al., 2021). If radiosounding relative humidity exceeded 95 %, a liquid water cloud was modeled in the respective vertical levels using a
140 modified adiabatic liquid water content approach following Karstens et al. (1994). To imitate the instrument's noise, a random noise factor was added to the simulated T_B taken as a random sample from a Gaussian distribution with standard deviation of 0.4K (Maschwitz et al., 2013). For the temperature retrieval, only a linear regression was used as in Walbröl et al. (2022). To derive temperature profiles from the elevation scans, coefficients c_1 and c_2 were calculated by adjusting the angle for which radiative transfer was performed. Theoretical LWP uncertainty scales with retrieved LWP, and is further discussed in Sec 6.3.
145 To further improve the LWP retrieval, a clear-sky offset correction method is applied to the retrieved LWP (van Meijgaard and Crewell, 2005; Ebell et al., 2017). The correction scheme identifies a liquid-free condition if the standard deviation of LWP in a running 2-minute window, as well as the previous and subsequent 2-minute window, is below $2.5 \, \text{gm}^{-2}$. The median LWP during the identified 2-minute clear-sky period is subsequently subtracted from all following LWP measurements until the next clear-sky period. Note that due to the statistical retrieval approach, negative (unphysical) LWP values can occur. Remaining
150 few negative LWP values are not set to zero to keep for statistical noise evaluation and to avoid biasing the overall statistical distribution of LWP. That way, the clear-sky LWP noise can be estimated by analyzing the LWP distribution in independently identified clear-sky periods as presented in Sec 6.3.

3.2 Single-channel 89 GHz

For the passive 89 GHz channel of the W-band cloud radars, a statistical retrieval is applied to derive LWP of the column
155 above the instrument from the observed brightness temperatures T_{B}. The difference in brightness temperature ΔT_{B} between
cloudy-sky T_{B} and the closest clear-sky $T_{\mathrm{B},0}$ observation is used in a third-order regression (Eq. 2) to estimate the LWP.

$$\mathrm{LWP} = a \cdot \Delta T_{\mathrm{B}} + b \cdot \Delta T_{\mathrm{B}}^2 + c \cdot \Delta T_{\mathrm{B}}^3 \text{ with } \Delta T_{\mathrm{B}} = T_{\mathrm{B}} - T_{\mathrm{B},0} \tag{2}$$

Instrument biases are reduced by using the difference in brightness temperatures, so that the unbiased portion of the signal
from LWP remains. The clear-sky brightness temperature is obtained by selecting profiles not showing any radar reflectivity.
160 Additionally, measurements up to 5 min after rain events were filtered out from the clear-sky set to avoid sections where
the radome might be still wet. The unknown coefficients of the regression (a, b, and c) are derived from a training data
set compiled of artificial LWPs and simulated brightness temperatures calculated with the forward model operator Passive
and Active Microwave TRAnsfer model (PAMTRA; Mech et al., 2020) on atmospheric profiles constructed from the 401
radiosondes launched on the research vessels (Merian 182, Meteor 219) and artificial clouds between 0 and 5 km with LWPs
165 up to 1 kgm^{-2}. To retrieve the LWP, the coefficients derived for the closest radiosounding were applied following Eq. 2 to ΔT_{B}
which was in turn noised by a random number of a Gaussian distribution with width of 0.5K. To exclude observations during
rain, filtering for those was performed by applying the rain flags contained in the data sets.

Clear-sky IWV is retrieved from the single channel T_{B} measurements as emissions then are dominated by water vapor. A
quadratic regression is applied as in Eq. 1, weighed by variability of T_{B} around the radiosonde launch. By applying a weight
170 to the regression, mis-identified clear-sky radiosoundings are excluded from the training. 120 and 65 clear-sky radiosoundings
were identified aboard the Meteor and Merian, respectively, by applying a 98 % relative humidity threshold, and were used
to derive the coefficients linking T_{B} and IWV. The retrieval was applied to clear-sky conditions as identified using a radar
reflectivity threshold of -50 dBZ.

4 Data Processing and Overview

175 This Section describes the processing of the data set as available on AERIS, doi.org/10.25326/454 (Schnitt et al., 2023).

Level 1 Level 1 files are provided for each instrument and include the unfiltered instrument output on original time resolution.
HATPRO measurements were processed by the MWR PRO software (see Sec 3.1), providing one daily file for IWV, LWP, T
and q retrieval as well as for the T_{B} measurements. Note that different LIMHAT retrieval output is available in (Kalesse-Los
et al., 2020). The HATPRO quality flags include flags for visual inspection, sun influence in measurement beam, and a T_{B}
180 threshold indicating poor measurement quality. For the W-band measurements, one file per day is produced by RPG software
(see Acquistapace et al., 2022).

Level 2 One Level 2 file is provided per instrument, concatenating the daily Level 1 HATPRO and hourly W-band files,
respectively, in one single file. Measurements and retrieval products are given in the original instrument's time resolution. LWP

is clear-sky corrected as described in Sec 3.1. The provided HATPRO quality mask indicates poor measurement and retrieval quality, respectively, combining single flags from Level 1 files in one flag. Poor measurement quality is given if any of the Level 1 quality flags is True, if episodes need to be excluded manually due to maintenance on the instruments (see Sec 2). An additional check is performed by simulating T_B for each channel individually based on T_B observations of all other channels. If the difference between simulated and observed T_B is above a certain threshold, the spectrum is considered as unphysical and flagged. These unphysical spectra can be caused by rain, wet radome, or other external sources (such as radio-frequency interference, sun in beam, etc.). Threshold values were determined empirically, and are as follows: at K-band the sum of the absolute differences between channels 2 through 7 is larger than 3 K; at V-band the sum of the absolute differences between all channels is larger than 7 K. Poor retrieval quality is flagged for IWV, LWP, temperature, and humidity independently. In addition to the information given by the instrument's housekeeping data, IWV values larger than $60\,\mathrm{kg\,m^{-2}}$, and LWP values larger than $1000\,\mathrm{g\,m^{-2}}$ are clipped (see e.g. Jacob et al. (2019)). LWP clipping amounts to 4.3 % (BCOHAT), 1.5 % (LIMHAT), 2.2 % (LIMRAD), 1.5 % (MSMRAD) of all available retrieved LWP.

Ground-based passive microwave radiometer measurements are not reliable during precipitation events due to additional liquid water emissions on the radome contributing to the column emissions. Flagging precipitation is, thus, crucial to guarantee a successful quality of the retrieved quantities. The HATPRO precipitation mask is set to True when precipitation was detected by the HATPRO weather station. At BCO, an independent weather station was additionally used to detect precipitation as the internal system broke (see Sec 2.1). Additional Ka-band zenith-pointing radar measurements (Hirsch, 2022) were used to improve precipitation detection, indicating precipitation if reflectivity at 250 m was above -50 dBZ. Aboard the Meteor and Merian, passive radiometer measurements were flagged for precipitation according to the simultaneous W-band radar measurements. Different conditions were used due to different radar chirp programs resulting in different sensitivity in the atmospheric boundary layer. Precipitation is flagged if any radar reflectivity larger than -40 dBZ occurred in range bins below 400 m (Meteor) or 250 m (Merian), if a radar reflectivity with more than 0 dBZ was detected in the atmospheric column, or if a rain-rate was sensed by the radar weather station.

As described in Sec 2, the HATPRO instruments performed different measurement strategies deviating from pure zenith measurements. A position mask included in Level 2 data indicates zenith measurement, azimuth scans, azimuth position (ocean or land) or elevation scan measurement. In order to obtain IWV from the single-channel 89 GHz measurements, clear-sky conditions are needed as identified by the simultaneous radar measurements. Clear-sky IWV is derived if no reflectivity above -50 dBZ occurred in the measurement column.

Level 3 One Level 3 file is provided for each site, combining all available radiometer and single-channel measurements on a mutual 3 s time grid to facilitate inter-platform comparison. A core measurement period was defined ranging from January 19 until February 14, 2020, during which all instruments were operational. As illustrated in Fig 2, certain days did not contain measurements due to maintenance, and precipitation reduced the amount of available measurements. Aboard the Meteor, HATPRO and Wband precipitation masks are combined to a single strict precipitation flag set to True if either instrument logged the occurrence of precipitation. Independent clear-sky measurements obtained from ceilometer observations were added to the BCO and Meteor data sets. A joint cloud mask derived from ceilometer and Ka- and W-band radar measurements indicates

whether conditions were clear, probably cloudy or confident cloudy (see Sec. 6.1). All following analyses, if not indicated
220 differently, are based on the Level 3 data set.
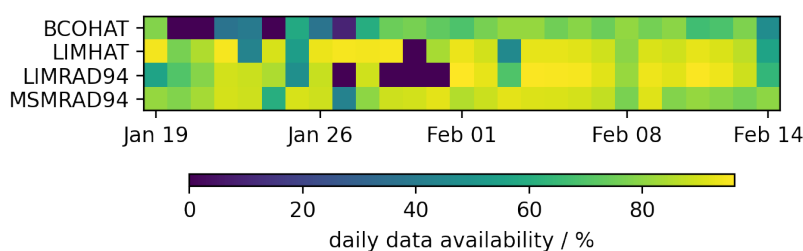
Figure 2. Timeline of measurement availability (color-coded, in percent) in the identified core period between January 19 and February 14, 2020, for each instrument. Percentages are calculated with respect to the optimal expected number of measurements on the 3 s temporal resolution grid.

Level 4 Quality-controlled time series of IWV, LWP, precipitation and cloud mask are given in one file for all three sites. Level 4 estimates are based on BCOHAT, LIMHAT, and MSMRAD retrieved IWV and LWP. Different files are provided for timelines sampled to different temporal resolution: 3 seconds (orginal), 1 minute, 30 minutes, 1,3, 6, 12 hours, and daily. The 6-hourly timeline of IWV, LWP, 6-hourly variability of LWP, as well as daily precipitation fraction are illustrated in Fig 3.
225 Spikes in LWP and LWP variability are related to unidentified precipitation events. While IWV varies little when sampled daily, longer sampling times smooth the LWP distribution.

Mean characteristics of the core period are summarized in Tab 2 as derived from the Level 4 3-second resolution data set. At BCO, aboard the Meteor, and the Merian, respectively, 5.7, 6.9 and 8.7 % of all measurement time steps were flagged as precipitating at ground. Scenes are flagged confident cloudy in 33.2, 27.5, 30.6 % of all valid measurements at BCO, Meteor
230 and Merian, and are characterized by a mean LWP of 66.5, 56.4 and 40.4 $\mathrm{g\,m^{-2}}$, respectively.
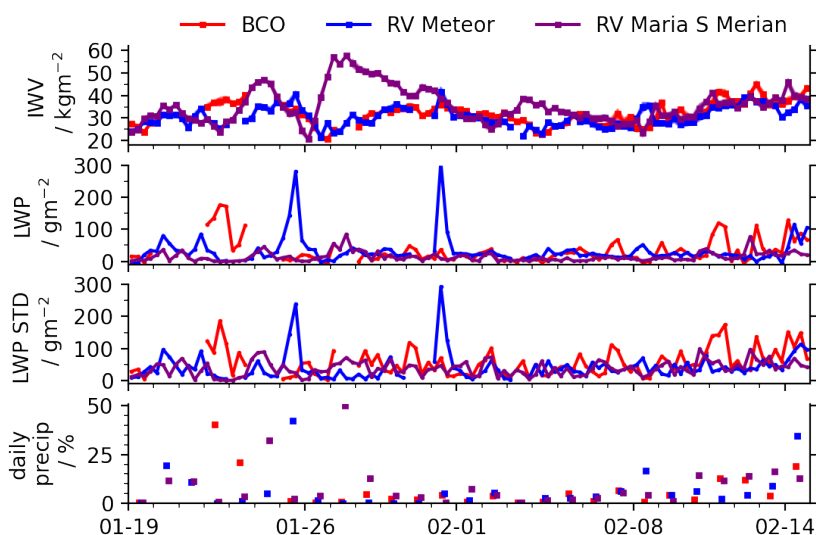
Figure 3. Timeline of 6-hourly (a) IWV, (b) LWP, (c) LWP standard deviation in a 6-hour window, (d) daily precipitation fraction, recorded at BCO (red), aboard the Meteor (blue) and Merian (purple).

Table 2. Characteristics of clouds, water vapor, precipitation and cloud occurrence at each site. Precipitation and cloud cover are calculated as temporal fraction of all valid measurements within the core period. Mean LWP is calculated for confident cloudy scenes.

site	mean IWV	confident cloudy	mean LWP	precip fraction
	kgm^{-2}	%	gm^{-2}	%
BCO	31.8	33.2	66.5	5.8
Meteor	30.3	27.5	56.4	6.9
Merian	33.3	30.6	40.4	8.7

5 Integrated Water Vapor

The IWV conditions measured at each site by each instrument are illustrated in Fig 4. Corresponding distribution parameters are summarized in Tab 3.

At BCO, a mean IWV of $31.8\,kgm^{-2}$ was measured in the core period with a standard deviation of $5.0\,kgm^{-2}$. The conditions measured aboard the Meteor agree within the associated uncertainty with a mean IWV of $30.3\,kgm^{-2}$, but show slightly less variability (standard deviation of $4.5\,kgm^{-2}$). The mean conditions aboard the Meteor measured by the LIMHAT and LIMRAD agree, while the LIMRAD IWV distribution is slightly narrower and less skewed due to the fact that the retrieval is only applied in clear-sky conditions. As the Merian was additionally sampling further South over warmer waters with deeper convection,

Table 3. Characteristics of IWV conditions measured by each instrument at each site, including number of valid non-precipitating measurements, mean IWV, median IWV, standard deviation (STD) and skewness of IWV probability distribution. Note that single-channel LIMRAD and MSMRAD IWV is retrieved for clear-sky conditions only.

site	N	mean IWV	median IWV	IWV STD	skewness
	-	kgm^{-2}	kgm^{-2}	kgm^{-2}	-
BCOHAT	411643	31.8	31.8	5.0	0.3
LIMHAT	629753	30.3	29.7	4.5	0.4
LIMRAD	396974	30.1	30.0	3.5	0.1
MSMRAD	448666	33.3	32.3	6.3	0.6

IWV conditions were moister with a mean IWV of $33.3\,kgm^{-2}$, hence larger skewness. The skewness of all distributions

240   indicates that the 2-month IWV conditions follow a lognormal distribution rather than a normal distribution which is also confirmed visually in Fig 4.
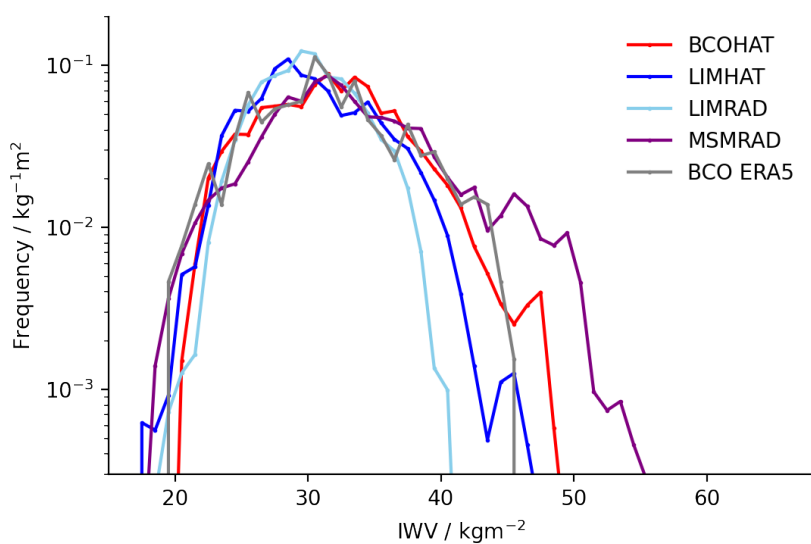
Figure 4. Frequency of Occurrence of IWV retrieved from HATPRO measurements at BCO (BCOHAT, red) and aboard Meteor (LIMHAT, blue), as well as from single-channel T_B aboard Meteor (LIMRAD, cyan) and Merian (MSMRAD, purple). The distribution of ERA5 values at BCO (gray) is added for comparison. Displayed frequencies are cut if calculated from less than 30 measurement points. Note that LIMRAD and MSMRAD IWV is only retrieved in clear-sky conditions.

These results align with the results by Foster et al. (2006) who find lognormal distributions in IWV at many locations worldwide, in particular in the (sub-)tropics. Compared to the dry season conditions observed during Narval-1 with a mean IWV of $28\,\mathrm{kg\,m}^{-2}$ (Jacob et al., 2019), EUREC^{4}A was slightly moister. The mean IWV of $33.2\,\mathrm{kg\,m}^{-2}$ measured by the HAMP

245   radiometers aboard HALO (Jacob et al., 2019) is higher than the ground-based estimates from Meteor which sampled a similar area which we relate to the different retrievals used.

We evaluate retrieved IWV by means of the root-mean-square-error (RMSE), Pearson correlation coefficient, and bias (independent measurement - MWR) with independent IWV measurements derived from radiosoundings (Stephan et al., 2021) and Global Navigation Satellite System (GNSS) (Bock et al., 2021; Bosser et al., 2021), and compare to ERA5 re-analysis data

250   (Fig 5 and Tab 4). MWR and radiosoundings are compared in a 10-minute window around each 4-hourly sounding launch to minimize radiosounding drifting effects when comparing to the zenith column. GNSS and MWR measurements are averaged and compared in 15 minute time windows matching GNSS realistic temporal resolution. For the ERA5 intercomparison, MWR measurements are resampled to the full hour.

Retrieved IWV is closely correlated with sounding IWV at all sites with correlation coefficients higher than 0.9. The RMSE

255   for the HATPRO measurements at BCO is $1.1\,\mathrm{kg\,m}^{-2}$, which is similar to the MWR-sounding RMSE that Steinke et al. (2015) find. The MWR measurements are on average drier than the radiosoundings' IWV as seen by the positive bias of $1.7\,\mathrm{kg\,m}^{-2}$. A similar bias of $1.6\,\mathrm{kg\,m}^{-2}$ is found in the LIMHAT - sounding comparison, although the RMSE is smaller than at BCO ($0.7\,\mathrm{kg\,m}^{-2}$). The dry bias between MWR measurements and radiosoundings at both BCO and Meteor could be related to the fact, that the statistical retrieval is trained on radiosoundings launched from Grantley International Airport. Bock et al. (2021)

260   find that the airport radiosoundings exhibit a dry bias of $2.9\,\mathrm{kg\,m}^{-2}$ compared to the Vaisala MW41 radiosoundings used at BCO during EUREC^{4}A (Stephan et al., 2021). Aboard the Meteor, the LIMHAT IWV data set can additionally be used to evaluate the dropsondes launched from HALO's circles (George et al., 2021) which were corrected for a dry bias compared to the radiosounding data set.

The MWR-sounding bias of clear-sky IWV retrieved from LIMRAD is reduced by $70\,\%$ compared to the respective HATPRO

265   derived IWV. The RMSE of LIMRAD - radiosoundings (1.3) is slightly smaller than at BCO, while, the Merian measurements' RMSE is higher than expected ($3.6\,\mathrm{kg\,m}^{-2}$). This increase in RMSE might be related to the lower number of radiosoundings used for training and evaluation which could also explain the switch of bias sign to negative values. Single- and multi-channel clear-sky IWV retrievals can be directly intercompared using simultaneous LIMRAD and LIMHAT measurements aboard the Meteor. All core period measurements agree with an RMSE of $1.2\,\mathrm{kg\,m}^{-2}$, affected by a bias of $1\,\mathrm{kg\,m}^{-2}$ with LIMRAD being

270   moister than LIMHAT.

At BCO, IWV obtained from GNSS and BCOHAT exhibit a RMSE of $1.4\,\mathrm{kg\,m}^{-2}$. As opposed to Bock et al. (2021), we do not find a bias between the measurements which could be attributed to different quality filtering mechanisms used in this analysis. Aboard the Meteor, the LIMHAT - GNSS RMSE is similar ($1.4\,\mathrm{kg\,m}^{-2}$) but affected by a negative bias of $-1.1\,\mathrm{kg\,m}^{-2}$ with GNSS measurements moister than the MWR measurements. Bosser et al. (2021) report that the GNSS measurements

275   aboard the Merian were of poor quality which explains the large RMSE and bias when comparing to MSMRAD IWV.

Table 4. Evaluation of MWR retrieved IWV from BCOHAT, LIMHAT, LIMRAD and MSMRAD using independent IWV measurements of radiosoundings, GNSS and closest ERA5 field through RMSE, bias and correlation coefficient. Note that LIMRAD and MSMRAD evaluation is performed in clear-sky conditions only.

		sounding	GNSS	ERA5
	N	125	2013	514
BCO	RMSE	1.1	1.4	2.2
BCOHAT	bias	1.7	-0.1	-1.0
	corr	0.99	0.96	0.90
	N	164	2377	427
Meteor	RMSE	0.7	1.5	2.3
LIMHAT	bias	1.6	-1.1	-0.1
	corr	0.99	0.95	0.86
	N	120	1805	401
Meteor	RMSE	1.3	1.8	2.4
LIMRAD	bias	0.5	-1.9	-0.6
	corr	0.97	0.90	0.8
	N	82	1632	392
Merian	RMSE	3.6	6.5	2.9
MSMRAD	bias	-0.5	-3.8	-1.3
	corr	0.91	0.72	0.93

The two periods of ship collocation (see Sec. 2.2) allows a direct comparison of clear-sky IWV derived from LIMRAD, LIMHAT and MSMRAD. Comparing the radars from both ships, LIMRAD and MSMRAD are associated with an RMSE of $1.1\,\mathrm{kg\,m^{-2}}$, a correlation coefficient of 0.88, and a bias of -0.3 (LIMRAD moister than MSMRAD). Given this good agreement, MSMRAD IWV seems more accurate than the GNSS measurements, and closes the measurement gap of highly temporally resolved IWV measurements aboard the Merian.

As MWR measurements were not assimilated into re-analysis, a comparison to re-analysis ERA5 fields closest in time and space can give further retrieval evaluation. Retrieved IWV and ERA5 RMSE at BCO and Meteor agree to within $2.5\,\mathrm{kg\,m^{-2}}$ with slightly higher agreement aboard the Merian ($2.9\,\mathrm{kg\,m^{-2}}$). While LIMHAT's IWV is unbiased compared to ERA5, a dry bias of $-1.0\,\mathrm{kg\,m^{-2}}$ and $-1.3\,\mathrm{kg\,m^{-2}}$ is seen at BCO and aboard Merian, respectively.
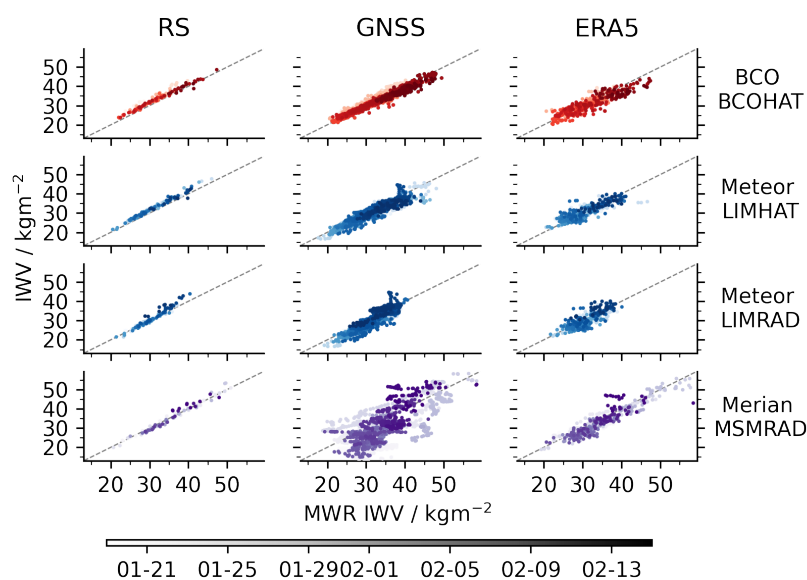
Figure 5. Pair-wise IWV evaluation of MWR retrieved IWV (x-axis) for four different instruments (rows) to independent measurements (y-axis) of radiosoundings (first column), GNSS (second column), ERA5 (third column), color-coded by time from January 19, 2020 (light) until February 14, 2020 (dark). Note that IWV from LIMRAD and MSMRAD is only available in clear-sky conditions.

6 Liquid Water Path

This section describes the Liquid Water Path (LWP) conditions estimated from measurements by the different instruments in non-precipitating conditions. Separating conditions in clear-sky and cloudy sky requires a cloud mask, which is built on independent measurements available from ceilometer and Ka-/W-band radar as further described in Sec 6.1. The resulting cloudy LWP conditions are analyzed in Sec 6.2. Clear-sky identified scenes serve as base to characterize the clear-sky LWP noise, contributing to the overall LWP uncertainty and detection limit analysis presented in Sec 6.3).

6.1 Cloud Mask

A cloud mask was derived for each site based on ceilometer and Ka-band radar, ceilometer and active LIMRAD, and active MSMRAD measurements, respectively, for BCO, Meteor and Merian. The ceilometer is flagged clear if no backscatter is recorded. Due to the different radar systems and sensitivities at each site, the radar-based cloud masking differs as follows. At BCO, a scene is flagged clear if no reflectivity was recorded between 500 m and 8 km to exclude mis-flagging of sea-spray affected scenes. Aboard the ships, the W-band cloud radar measurements are flagged clear if no reflectivity above a threshold of -50 dBZ was recorded in the column above the instrument.

A joint cloud mask at BCO and Meteor identifies scenes as *clear* if both ceilometer and radar flags are clear. Scenes are flagged as *probably cloudy* if either ceilometer or radar sensed a cloud. These occurrences are mainly due to sensor beam

Table 5. Cloud Mask Characteristics at BCO, aboard the Meteor and Merian. Scenes are *clear* if both ceilometer and radar sensed clear-sky; *probably cloudy* if either detected a cloud; and *confident cloudy* if both radar and ceilometer detected clouds. Percentages are relative to total number of non-precipitating measurement points with valid LWP and cloud mask.

site	clear %	probably cloudy %	confident cloudy %
BCOHAT	45.8	21.0	33.2
LIMHAT	57.0	15.5	27.5
LIMRAD	59.8	14.9	25.3
MSMRAD	69.4	0	30.6

300   mismatch, platform motions, or sensitivity differences between the ceilometer and radar (see discussion in Konow et al., 2021). *Confident cloudy* scenes refer to measurements in which both radar and ceilometer sensed a cloud. Aboard the Merian, scenes were classified as clear or confident cloudy based on MSMRAD.

3.7 %, 20 % and 8.2 % of all mesaurements were excluded at BCO, Meteor, Merian, respectively, due to missing data of ceilometer or radar. The comparatively higher percentage aboard the Meteor is dominated by data availability of LIMRAD.

305   For further LWP analyis, we demand a valid LWP and a valid cloud mask for a measurement to be considered, thus excluding scenes affected by precipitation or MWR measurement quality. This reduces the availability of points to 50.5, 66.8, 69.5, and 83.1 % of all 3 s measurements in the core period, dominated by instrument availability shown in Fig 2. Table 5 summarizes the respective cloud cover fractions of clear, probably cloudy and cloudy scenes relative to this subsample for all instruments. Clear-sky fraction is highest aboard the Merian, and lowest at BCO. We relate the highest clear-sky fraction of 69.4 % aboard

310   the Merian to the missing ceilometer and reduced sensitivity of the radar to optically thin and geometrically small clouds (Mieslinger et al., 2022).

Compared to the airborne cloud cover products presented in Konow et al. (2021), the here presented ground-based derived confident cloudy cloud cover estimates are closest to the airborne lidar-derived cloud cover of 34 %. Differences arise due to the fact that airborne operation was limited to selected days and daytime, and that airborne horizontal resolution is lower than

315   when measured from ground. Here presented cloud cover matches the cloud cover found at BCO from 2 years of measurements (Nuijens et al., 2014).

6.2 Cloudy LWP

Fig 6 illustrates retrieved LWP distributions observed by BCOHAT, LIMHAT, LIMRAD and MSMRAD in confident cloudy scenes. Corresponding distribution parameters are given in Tab 6.

320   Mean LWP conditions at BCO, aboard the Meteor and Merian were 66.5, 56.4, 46.4 and 40.4 $\mathrm{gm^{-2}}$. The mean conditions at BCO and Meteor align well with the mean airborne LWP of 63 $\mathrm{gm^{-2}}$ found during NARVAL-1 observed the same region in
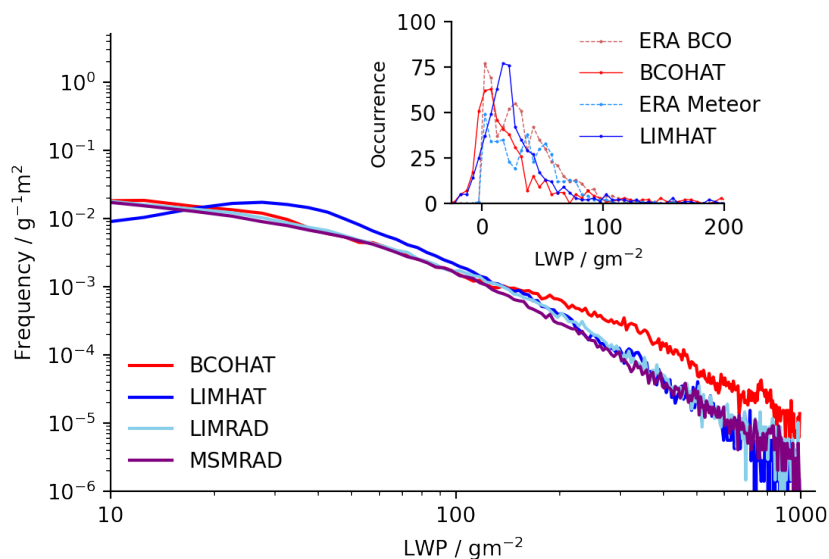
Figure 6. Distribution of LWP occurrence in confident cloudy, non-precipitating scenes at BCO (red), aboard the Meteor retrieved from LIMHAT (blue) and LIMRAD (cyan) measurements, as well as aboard the Merian with MSMRAD (purple). The inlet displays the distribution of LWP re-sampled to the full hour from BCOHAT (red, solid) and LIMHAT (blue, solid), and the corresponding hourly-resolved ERA5 total column liquid water (dashed).

Table 6. Characteristics of non-precipitating LWP distribution, including mean, median, standard deviation, 10th and 90th percentile, skewness, as retrieved from BCOHAT, LIMHAT, LIMRAD and MSMRAD in confident cloudy (confident and probably cloudy) identified scenes.

site	cloud cover	mean	median	standard dev	10th	90th	skewness
	%	gm^{-2}	gm^{-2}	gm^{-2}	gm^{-2}	gm^{-2}	-
BCOHAT	33.2 (54.2)	66.5 (46.4)	27.6 (16.6)	110.1 (93.4)	2.2 (-1.8)	179.9 (121.0)	3.6 (4.4)
LIMHAT	27.5 (43.0)	56.4 (41.8)	37.5 (26.3)	67.4 (58.0)	11.5 (4.8)	117.8 (90.5)	4.4 (5.0)
LIMRAD	25.3 (40.2)	46.4 (29.8)	22.7 (8.1)	74.5 (63.2)	0.6 (-1.7)	116.8 (83.4)	4.5 (5.3)
MSMRAD	30.6	40.4	18.3	71.1	-0.9	102.4	4.9

similar dry winter trade conditions (Jacob et al., 2019; Schnitt et al., 2017). As BCOHAT and LIMHAT retrieved mean LWP of 66.5 gm^{-2} and 56.4 gm^{-2} agree within their associated LWP uncertainties (see Sec 6.3), it can be assumed that BCO and Meteor were on average exposed to similar cloud conditions driven by the trade-winds. Median and mean LWP differ as the mean LWP is influenced by single events of high LWP, e.g. through un-flagged precipitation or sea-spray, while the median is driven by the large amount of small LWP below the instruments' detection limit.

90 % of observed confident cloudy columns were associated with a LWP of less than 180, 120 and $103 \, \mathrm{g m^{-2}}$ at BCO, and aboard the Meteor and Merian, respectively. The higher 90th percentile as well as a higher LWP standard deviation of $110.1 \, \mathrm{g m^{-2}}$ at BCO are most probably related to wet radome conditions as the blower unit of BCOHAT was broken throughout

330   most of the core period (as opposed to the other instruments). We also suspect that the sea-spray altered, aged radome was less hygroscopic compared to the newer LIMHAT radome, leading to additional moisture on the radome and longer drying times. An additional island impact triggering deeper convection in prevailing non-trade-wind conditions is in ongoing analysis. The negative values of the 10th percentile reflect the fact that the statistical regression covers negative values to avoid biasing the overall distribution (see Sec 3.1), and indicates that the cloud mask did not perform well in all conditions. Likely, the wider

335   field of view of the MWR compared to the active remote sensing instruments used for the cloud mask led to mis-identification of scenes.

Expanding the analysis to include *probably cloudy* conditions reduces mean and median LWP, as well as all other parameters of the distribution given in Tab 6, likely due to the fact that more mis-flagged clear-sky conditions impact the LWP distribution. This shift in distribution parameters illustrates the sensitivity of the derived LWP properties to the cloud mask performance.

340   At BCO and Meteor, retrieved LWP is compared to the ERA5 estimates by resampling BCOHAT and LIMHAT's LWP, respectively, to every hour (see inlet in Fig 6). Instrument-derived mean LWP of 33.6 and $39.6 \, \mathrm{g m^{-2}}$ agree well with ERA5 mean LWP of $34.5 \, \mathrm{g m^{-2}}$ and 36.0 at BCO and Meteor, respectively. The measured LWP variability, here quantified as standard deviation, of 58.3 and $84.7 \, \mathrm{g m^{-2}}$ is higher than the ERA5 variability of 27.9 and 26.4, respectively, which we attribute to the horizontal resolution of ERA and the small cloud sizes.

345   ## 6.3   LWP Uncertainty and Detection Limit

Characterizing the uncertainty of the retrieved LWP by independent measurements is not straight forward as LWP retrieved from measurements by visible or infrared remote sensing techniques is not sensitive to the same column as the microwave measurements. Therefore, a clear-sky LWP noise can be derived by analyzing retrieved LWP in independently classified clear-sky cases as a generally accepted strategy (Jacob et al., 2019; van Meijgaard and Crewell, 2005). Retrieval offsets to zero are

350   due to the statistical nature of the retrieval approach, due to calibration artefacts, and radiometric noise. The lowest detectable LWP is then calculated from the clear-sky LWP noise for different water vapor conditions. Cloudy-sky LWP uncertainty can be estimated as a function of LWP by calculating a root-mean-square difference (RMSD) of true vs retrieved LWP. True LWP here refers to the LWP used to forward-model T_{B} in the radiative transfer calculations (see Sec 3), while retrieved LWP is the result of applying the retrieval equation to the same T_{B}.

355   The retrieved clear-sky LWP distribution at BCO is illustrated in Fig 7a, and Tab 7 summarizes the distribution characteristics for all sites. 45.8, 57.0, 59.8 and 69.4 % of all valid LWP BCOHAT, LIMHAT, LIMRAD and MSMRAD measurements, respectively, are identified as clear-sky. Note that the fractions disagree for LIMRAD and LIMHAT aboard the Meteor due to different data gaps in the measurements. Applying a Gaussian fit to the distribution yields to a mean and standard deviation, which is interpreted as clear-sky LWP bias and clear-sky LWP noise, respectively. The Gaussian fit widths of $10.2 \, \mathrm{g m^{-2}}$ and

360    $11.7 \, \mathrm{g m^{-2}}$ for BCOHAT and LIMHAT, respectively, quantify the clear-sky LWP noise, and match clear-sky noises previously

Table 7. Parameters of clear-sky LWP distribution at all sites, including clear-sky fraction of all valid LWP measurements, median, mean, standard deviation, 10th and 90th percentile. Additionally, mean and standard deviation of a Gaussian fit are given.

site	clear-sky	median	mean	standard dev	10th	90th	fit mean	fit standard dev
	%	gm^{-2}	gm^{-2}	gm^{-2}	gm^{-2}	gm^{-2}	gm^{-2}	gm^{-2}
BCOHAT	45.8	4.9	2.4	25.4	-9.0	17.3	3.0	10.2
LIMHAT	57.0	10.3	11.4	11.7	-5.5	23.7	10.3	11.7
LIMRAD	59.8	-0.4	0.0	4.0	-3.1	1.1	-0.4	3.4
MSMRAD	69.4	0.2	0.0	8.1	-4.6	3.9	-0.2	4.3

Table 8. Characteristics of confident cloudy Level 3 LWP distribution considering each instrument's detection limit. Fraction (relative to all valid confident cloudy measurements) and mean LWP are calculated for the following LWP bins: LWP below detection threshold, LWP between detection threshold and $30\,gm^{-2}$, LWP between 30 and $100\,gm^{-2}$, and LWP above $100\,gm^{-2}$.

	detection limit	LWP < detect		detect < LWP < 30		30 < LWP < 100		LWP > 100	
		fraction	mean	fraction	mean	fraction	mean	fraction	mean
	gm^{-2}	%	gm^{-2}	%	gm^{-2}	%	gm^{-2}	%	gm^{-2}
BCOHAT	10.2	23.6	2.0	29.2	19.2	29.1	54.7	18.1	245.7
LIMHAT	11.7	10.2	3.5	28.0	21.6	48.7	52.7	13.2	185.1
LIMRAD	3.4	17.3	-1.3	40.6	14.6	29.5	55.1	12.6	193.4
MSMRAD	4.3	26.1	-1.9	36.0	14.9	27.6	55.5	10.4	195.0

identified for retrievals based on the similar channels (Jacob et al., 2019; Schnitt et al., 2017). The single-channel clear-sky LWP noises are smaller (3.9 and $4.3\,gm^{-2}$, respectively), as the retrieval approach is based on the T_{B} difference of cloudy and clear-sky. The lowest detectable LWP depends on the vertical water vapor distribution which, in cloudy conditions, is not available from any of the sites. Therefore, we estimate the smallest detectable LWP as the clear-sky LWP noise which, in turn,

365   depends on the performance of the independent cloud masking algorithm.

76.4, 89.8, 82.7 and 73.9 % of all confident cloudy flagged measurements are above the respective detection limits of BCO-HAT, LIMHAT, LIMRAD and MSMRAD (see Tab 8). The remaining undetected LWP compared to the ceilometer-radar cloud mask is most likely associated to optically thin clouds with low water contents (e.g. Mieslinger et al., 2022) and to cloud mask performance. This reduction in cloud cover when derived from passive microwave sensors is also observed by the airborne

370   cloud masks (Konow et al., 2021). One third of detected LWP is seen between detection limit and $30\,gm^{-2}$, as well as between 30 and $100\,gm^{-2}$, averaging to mean LWP conditions of 15 to $20\,gm^{-2}$ and around $55\,gm^{-2}$, respectively. Less than 20 and 15 % of detected LWP at BCO and aboard the ships, respectively, is associated with thicker clouds of higher than $100\,gm^{-2}$.
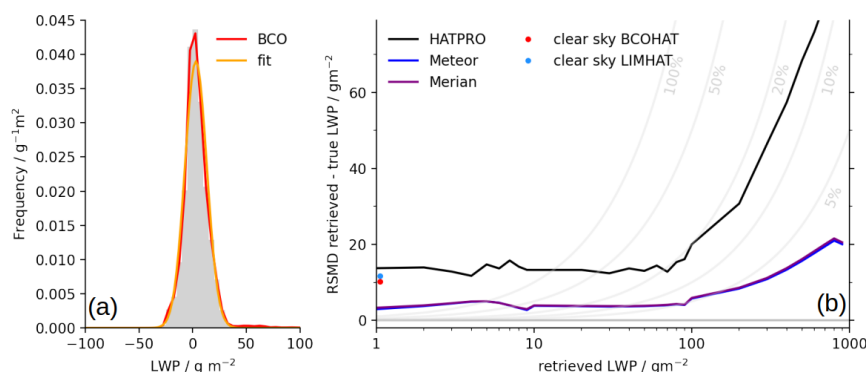
Figure 7. (a) Distribution of occurrence of BCOHAT LWP in clear-sky identified scenes (red) and respective Gaussian fit (orange), and (b) RMSD of retrieved vs true LWP for HATPRO (black) and single-channel retrieval (purple, blue), binned to retrieved LWP. Respective clear-sky Gaussian standard deviations are given for BCOHAT (red) and LIMHAT (blue).

Cloudy LWP uncertainty varies as function of retrieved LWP as illustrated in Fig 7b) binned to logarithmic bins of LWP. The mean RMSD for HATPRO derived LWPs below $20\,\mathrm{g\,m^{-2}}$ varies below $5\,\mathrm{g\,m^{-2}}$, corresponding to a relative RMSD between 375 75 and 50 %. For LWP between 20 and $100\,\mathrm{g\,m^{-2}}$, the RMSD moderately reduces from 50 to 15 % of retrieved LWP (15.8 at $50\,\mathrm{g\,m^{-2}}$). Above LWP of $100\,\mathrm{g\,m^{-2}}$, the relative uncertainty is better than 15 % (e.g. $29.9\,\mathrm{g\,m^{-2}}$ at LWP of $200\,\mathrm{g\,m^{-2}}$). High LWP values are in reality often affected by precipitation and, thus, not sensed by ground-/ship-based MWR measurements. Jacob et al. (2019) find on average higher RMSDs which we relate to the additional uncertainty given by the background emission characterization for airborne LWP retrieval.

380 The single-channel retrieval, different in retrieval design and training data set compared to the multi-channel retrieval, is characterized by lower uncertainties and detection limit. Higher liquid water emissions in the 89 GHz channel compared to the 31.4 GHz channel used in the multi-frequency HATPRO retrieval leads to a higher sensitivity of the retrieval to smaller clouds with less liquid. This retrieval, however, strongly depends on the knowledge of IWV conditions and accuracte clear-sky flagging. To be consistent between Meteor and BCO in terms of cloud sensitivity, the LWP time series provided in Level 4 is 385 based on LIMHAT LWP.

The availability of both multi- and single-channel retrieval aboard the Meteor allows a direct comparison of the two different retrieval approaches. A direct intercomparison reveals a RMSE of $25.7\,\mathrm{g\,m^{-2}}$, a bias of $-9.4\,\mathrm{g\,m^{-2}}$, and a high correlation of 0.92 (not shown). As LWP varies strongly in time and space, and sensors's fields of view are different, comparing the cloudy LWP distributions through percentiles is a preferable method. The percentiles of the cloudy LWP distribution of LIMRAD and 390 LIMHAT, illustrated in Fig 8, show that LIMRAD-retrieved LWP is skewed to lower values compared to LIMHAT's LWP. The different clear-sky correction approaches in the two retrievals constitute themselves in the fact that 14th to 26th percentiles are
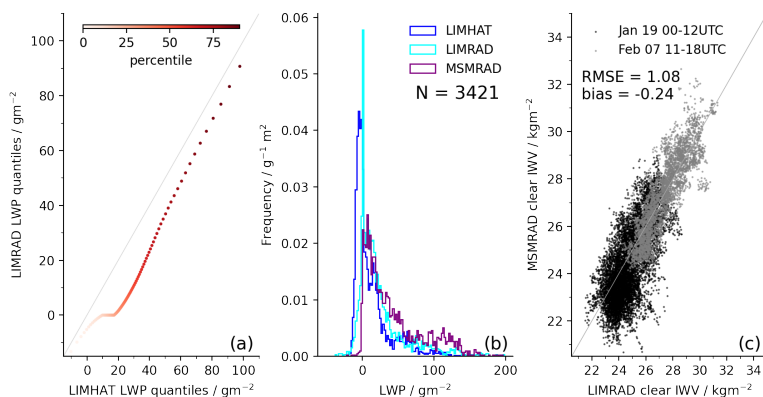
Figure 8. (a) Percentiles of LIMHAT vs LIMRAD retrieved cloudy LWP distributions during EUREC[4]A core period. Intercomparison of LIMRAD and MSMRAD retrieved (b) LWP and (c) clear-sky IWV when Meteor and Merian steamed along the same trajectory (January 19, 2020, 00-12UTC), and measured at the same location (February 07, 2020, 11-18UTC).

0 in LIMRAD, while they moderately increase up to $17.0\,\mathrm{gm}^{-2}$ in LIMHAT's distribution. Above $17\,\mathrm{gm}^{-2}$, a negative bias towards LIMRAD showing less LWP than LIMHAT moderately decreases towards higher LWP values.

Inter-platform evaluation of single-channel retrieved LWP and clear-sky IWV is performed for the two periods of ship
395 collocation (see 2.2). LWP obtained from LIMHAT, LIMRAD and MSMRAD are intercompared in a statistical way rather than directly as clouds might overpass with an unknown time shift.

Both LIMRAD and MSMRAD exhibit larger LWPs (median of 13.4 and $28.3\,\mathrm{gm}^{-2}$, respectively) than LIMHAT (1.9), confirming the percentile based comparison of LIMRAD and LIMHAT. Cloudy profiles of above $100\,\mathrm{gm}^{-2}$ were mostly seen by MSMRAD, which, however, might be related to single events that did not overpass the Meteor given the small sample
400 size. Yet, both radars were operated with different chirp table settings, leading to different sensitivity to boundary layer clouds which, in turn, might affect the performance of the cloud mask. Given the uncertainties of each LWP product identified above and the uncertainty related to the applied cloud mask, the distributions match well and are suitable for site intercomparison. Clear-sky IWV, less variable in space and time, is compared point to point, and exhibits a RMSE of 1.1 and a bias of $-0.2\,\mathrm{kgm}^{-2}$ (MSMRAD slightly drier). Both single-channel retrievals agree within the expected uncertainties.

405 Assuming that BCO and Meteor were exposed to similar conditions and given the fact, that multi-channel derived LWP is generally more reliable, we conclude that the LIMHAT measurements should be used as 'truth' for the Meteor site compared to the single-channel LIMRAD LWP. While LIMRAD single-channel LWP is biased by $-9.4\,\mathrm{gm}^{-2}$ compared to the multi-channel LWP estimates, presumably due to a higher sensitivity towards smaller clouds, this bias cannot be directly translated to MSMRAD LWP due to absolute calibration differences of the two cloud radars. Clear-sky T_{B} are affected by a RMSE of
410 2.6K, a bias of 5.5K (Merian warmer), but correlation of 0.67 is low due to temporal spatial mismatch. Given this T_{B} bias and assuming all other instrument characteristics being the same between LIMRAD and MSMRAD, Merian single-channel LWPs

might in reality be lower. An extended analysis can help to quantify this bias, e.g. by comparing similar looking clouds as seen in the active cloud radar part.

7 Thermodynamical profiles

415 The multi-channel measurements by the HATPRO instruments are used to retrieve temperature (see Sec 7.1) and absolute humidity (see Sec 7.2) profiles at BCO and aboard the Meteor, respectively. Temperature profiles are obtained from zenith measurements and when elevation scans were performed (see Sec 3.1), while absolute humidity profiles are only available in zenith mode. Profiles are obtained on 43 height levels with vertical resolution decreasing from 50-100 m in the moist layer to 200-500 m above the trade inversion.

420 We use the EUREC⁴A sounding data set (Stephan et al., 2021) to evaluate the MWR retrieved profiles, assuming that the radiosoundings represent the best estimate of the true atmospheric conditions. To compare radiosoundings and MWR, we interpolate the radiosoundings to the MWR height grid and average MWR measurements 5 minutes around each sounding launch as conditions in the Tropics change on longer timescales. 182 and 219 radiosoundings are used for BCO and Meteor, respectively. We then calculate RMSE and bias for each MWR height level. Positive biases here indicates an overestimation of
425 MWR compared to sounding value.

7.1 Temperature

The obtained temperature RMSE and bias are illustrated in Fig 9. At both sites, zenith mode RMSE increases throughout the moist layer from less than 0.5 K below Lifting Condensation Level (LCL) to 1.5 K at the trade inversion around 2 km.

As zenith HATPRO measurements generally contain 2 degrees of freedom (independent pieces of information), the retrieval
430 information content is too low to resolve the trade temperature inversion. Rather, the MWR profiles smooth the inversion, resulting in on average warmer MWR conditions at the base of the inversion, and colder conditions at inversion top, similar to conditions found in the Arctic (Walbröl et al., 2022). Temperature information content is highest below 4 km (Löhnert and Maier, 2012), which makes the MWR insensitive to the conditions in the middle troposphere as seen by further increasing RMSE.

435 Elevation scans have been shown to improve the derived temperature profile in the lowest kilometer of the boundary layer (Crewell and Lohnert, 2007; Walbröl et al., 2022). As illustrated in Fig 9, however, the BCOHAT and LIMHAT scans increase RMSE and bias in the layers below 1 km. We suspect that the GAIA sounding data set used for training is impacted by the island surface, leading to warmer temperatures in the moist layer compared to the zenith column at BCO or over the ocean. Typically, when trade winds prevail, radiosoundings launched at GAIA or BCO drift westwards over the island when ascending
440 through the sub-cloud layer. Paired with small seasonal temperature variations in the Tropics and, thus, little variability in the temperature training data set, this systematic training error translates into warm temperature biases of the retrieved temperature profiles compared to the launched radiosoundings. Elevation scans aboard the Meteor, and therein in particular the low
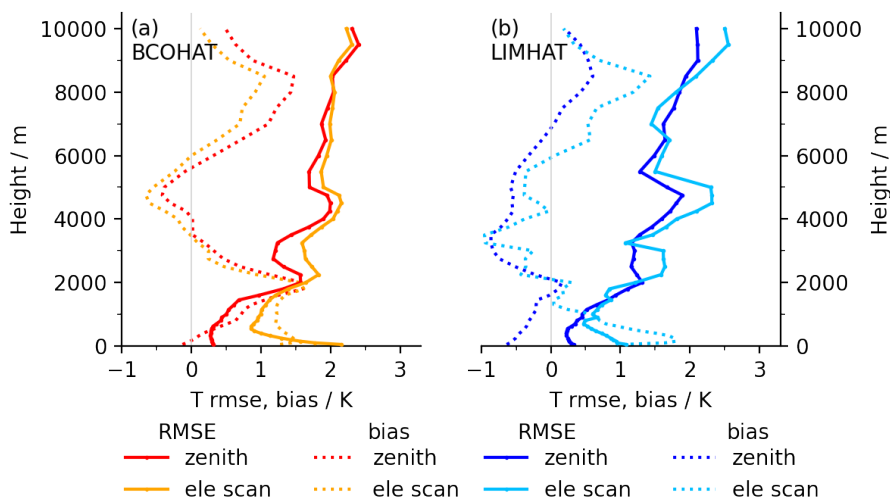
Figure 9. RMSE (solid) and bias (dashed) of (a) BCOHAT and (b) LIMHAT temperature profiles from zenith (blue; red) and elevation scan (orange; cyan) operation compared to simultaneous sounding profiles.

elevation angle measurements, are additionally affected by ship motion as LIMHAT was not stabilized. The functionality of the HATPRO-attached weather station might additionally impact the quality of the temperature retrieval.

445 ## 7.2 Absolute Humidity

Comparing radiosoundings and MWR yields to the RMSE and bias illustrated in Fig 10(a). At both sites, the RMSE from ground to LCL is $1.3\,\mathrm{g\,m^{-3}}$, and increases to $2.5\,\mathrm{g\,m^{-3}}$ in the area of the hydrolapse associated with the trade inversion. The tendencies of the bias can be further understood when analyzing the mean profiles as illustrated in Fig 10(b). From ground towards hydrolapse, MWR underestimates the humidity, resulting in a negative bias of $-1\,\mathrm{g\,m^{-3}}$. Throughout the hydrolapse,

450 MWR and sounding profiles converge, which is due to the smoothing of the MWR profile. Depending on the strength of the hydrolapse, MWR overestimates the humidity in the dry layer balancing the overall profile to match overall IWV conditions. Above the hydrolapse in the free troposphere, dry conditions prevail, and MWR is not sensitive to elevated moist layers. While the MWR covers the variability of moist layer water vapor well as seen by similar standard deviations of sounding and MWR profile, it does not resolve the variability in the hydrolapse or free troposphere. The overall negative bias in the absolute

455 humidity profile translates into a dry bias in the IWV estimate (compared to the radiosoundings) which confirms the findings in Sec 5.
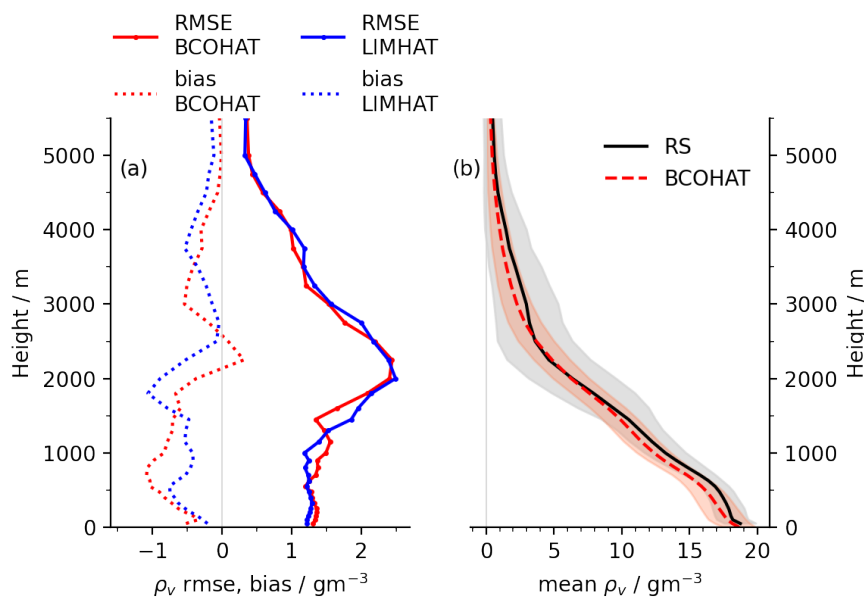
Figure 10. (a) BCOHAT (red) and LIMHAT (blue) RMSE (solid) and bias (dashed) of retrieved absolute humidity ρ_v profiles compared to simultaneous sounding profiles, and (b) mean ρ_v profiles of radiosoundings (black) and BCOHAT (red), shaded by their respective standard deviation.

8   Conclusions

This study presents the ground- and ship-based passive MWR measurements performed during the EUREC^{4}A field study. Between January 19 and February 14, 2020, continuous measurements of IWV, LWP, and coarse profiles of temperature

460   and absolute humidity were obtained in the vicinity of Barbados at 3 second resolution. 14-channel MWR measurements were performed at Barbados Cloud Observatory and aboard the Meteor with a HATPRO microwave radiometer, while single-channel measurements were performed at 89 GHz aboard the Meteor and the Merian complementing W-band cloud radar measurements.

The here presented data set contributes key measurements to study the coupling of clouds to cirulcation and their environ-
465   ment, the overall goal of the EUREC^{4}A field study (Bony et al., 2017; Stevens et al., 2021). The data set enables a continuous quantification of clouds' LWP in their immediate moisture environment, enables the characterization along spatial scales across the trade-driven Tropical Atlantic, and complements the airborne LWP measurements performed aboard HALO and the SAFIRE ATR42.

Similar mean IWV conditions of 31.8 and 30.3 kg m^{-2} at BCO and aboard the Meteor, respectively, support the hypothesis
470   that similar air masses were observed, evolving from Meteor towards BCO along the trade-wind driven region. The Merian sampled moister conditions on its track southward, leading to mean IWV conditions of 33.3 kg m^{-2}. The multi-channel retrieved

IWV at BCO is affected by a RMSE of 1.1, 1.4 and $2.2\,\mathrm{kgm^{-2}}$ compared to radiosoundings, GNSS and ERA5 estimates, matching uncertainties identified in mid-latitudes (Steinke et al., 2015).

A precipitation and cloud mask are included in the data set, as derived from an attached weather station and simultaneous cloud radar and ceilometer measurements. We find that 5.8, 6.9 and 8.7 % of all measurements contain ground-reaching precipitation at BCO, Meteor, Merian, respectively. Confident cloudy scenes prevail in 33.2, 27.5 and 30.6 % of available profiles, respectively, matching cloud cover estimates in Nuijens et al. (2014). Confident cloudy LWP distributions reveal a mean LWP of 66.5, 56.4 and $40.4\,\mathrm{gm^{-2}}$ at BCO, Meteor and Merian, respectively. 90 % of all confident cloudy profiles contained less than 180 and $120\,\mathrm{gm^{-2}}$ LWP at BCO and aboard the Meteor and Merian, respectively. Derived LWP statistics strongly depend on the performance of the cloud masking algorithm. When including probably cloudy identified scenes in the statistics, mean LWP and percentiles reduce by 30 % due to beam mismatches and resulting mis-identification of clear scenes.

Multi-channel retrieved LWP at BCO and aboard the Meteor is provided with an uncertainty of 30 % at $50\,\mathrm{gm^{-2}}$ and better than 15 % above $100\,\mathrm{gm^{-2}}$. Single-channel retrieved LWP uncertainty is reduced by 70 % at $50\,\mathrm{gm^{-2}}$ but might in reality be higher as the retrieval requires accurate quantification of IWV and clear-sky identification. Clear-sky LWP noise reveals a detection limit of 10.2, 11.7, 3.4 and 4.3 $\mathrm{gm^{-2}}$ for BCOHAT, LIMHAT, LIMRAD and MSMRAD. Up to 30 % of confident cloudy tagged profiles are below the LWP detection limit presumably due to undetected optically thin clouds (Mieslinger et al., 2022).

We recommend using the Level 4 data set for non-expert users as no additional flags need to be applied to the provided IWV and LWP time series. Data are re-sampled to different temporal resolutions, facilitating model-observation intercomparison. More experienced users will find more details in the Level 3 data set, including the temperature and humidity retrieval output. Future retrieval approaches could combine HATPRO and 89 GHz channel (Crewell and Löhnert, 2003) to advance the retrieval performance, especially also by applying neural-network based retrieval approaches (Jacob et al., 2019; Cadeddu et al., 2009). The single-channel LWP retrieval can be used to evaluate the approach presented by Billault-Roux and Berne (2021). The spatial dimension of this data set can be further exploited to characterize LWP and IWV conditions in different mesoscale organization conditions (e.g. Schulz et al., 2021), and to evaluate microwave and vis/IR satellite LWP products as well as climatologies (Elsaesser et al., 2017). Combining BCO and Meteor measurements can frame Lagrangian trajectory analyses targeting the evolution of air masses along the trade winds. Using this data set to benchmark cloud-resolving simulations will help to answer some of the central questions targeted by the EUREC[4]A field study on the interplay of clouds, circulation, convection and climate.

9 Data availability

The presented data set is available through AERIS, https://doi.org/10.25326/454 (Schnitt et al., 2023).

Author contributions.

SaS led the study, developed the Barbados-specific HATPRO retrieval, and prepared data set, manuscript and figures. AF and HKL supported the conceptualization of the study and led the Meteor measurements and post-processing, supported by
505 JR. MM and SC developed and ran the single-channel retrieval. CA led the measurements aboard the Merian. UL provided expertise on HATPRO retrieval and BP contributed the spectral flagging retrieval. FJ maintains the BCO measurements. BS led the EUREC4A campaign. All authors contributed to the manuscript.

Competing interests.   The authors have no competing interests.

Acknowledgements.   The data used in this publication was gathered in the EUREC4A field campaign and is made available through University
510 of Cologne, University Leizpig, Max Planck Institute for Meteorology. EUREC4A is funded with support of the European Research Council (ERC), the Max Planck Society (MPG), the German Research Foundation (DFG), the German Meteorological Weather Service (DWD) and the German Aerospace Center (DLR). SaS' EUREC4A participating was funded by a travel grant from Graduate School of Geosciences (GSGS) University of Cologne. We thank the BCO team for maintaining the observatory, and the AERIS team for their support in publishing the data set.

References

Acquistapace, C., Coulter, R., Crewell, S., Garcia-Benadi, A., Gierens, R., Labbri, G., Myagkov, A., Risse, N., and Schween, J. H.: EUREC[4]A's *Maria S. Merian* ship-based cloud and micro rain radar observations of clouds and precipitation, Earth System Science Data, 14, 33–55, https://doi.org/10.5194/essd-14-33-2022, 2022.

Billault-Roux, A.-C. and Berne, A.: Integrated water vapor and liquid water path retrieval using a single-channel radiometer, Atmospheric Measurement Techniques, 14, 2749–2769, https://doi.org/10.5194/amt-14-2749-2021, 2021.

Bock, O., Bosser, P., Flamant, C., Doerflinger, E., Jansen, F., Fages, R., Bony, S., and Schnitt, S.: Integrated water vapour observations in the Caribbean arc from a network of ground-based GNSS receivers during EUREC[4]A, Earth System Science Data, 13, 2407–2436, https://doi.org/10.5194/essd-13-2407-2021, 2021.

Bony, S., Stevens, B., Frierson, D. M. W., Jakob, C., Kageyama, M., Pincus, R., Shepherd, T. G., Sherwood, S. C., Siebesma, A. P., Sobel, A. H., Watanabe, M., and Webb, M. J.: Clouds, circulation and climate sensitivity, Nature Geoscience, 8, 261–268, https://doi.org/10.1038/ngeo2398, 2015.

Bony, S., Stevens, B., Ament, F., Bigorre, S., Chazette, P., Crewell, S., Delanoë, J., Emanuel, K., Farrell, D., Flamant, C., Gross, S., Hirsch, L., Karstensen, J., Mayer, B., Nuijens, L., Ruppert, J. H., Sandu, I., Siebesma, P., Speich, S., Szczap, F., Totems, J., Vogel, R., Wendisch, M., and Wirth, M.: EUREC4A: A Field Campaign to Elucidate the Couplings Between Clouds, Convection and Circulation, Surveys in Geophysics, 38, 1529–1568, https://doi.org/10.1007/s10712-017-9428-0, 2017.

Bony, S., Lothon, M., Delanoë, J., Coutris, P., Etienne, J.-C., Aemisegger, F., Albright, A. L., André, T., Bellec, H., Baron, A., Bourdinot, J.-F., Brilouet, P.-E., Bourdon, A., Canonici, J.-C., Caudoux, C., Chazette, P., Cluzeau, M., Cornet, C., Desbios, J.-P., Duchanoy, D., Flamant, C., Fildier, B., Gourbeyre, C., Guiraud, L., Jiang, T., Lainard, C., Le Gac, C., Lendroit, C., Lernould, J., Perrin, T., Pouvesle, F., Richard, P., Rochetin, N., Salaün, K., Schwarzenboeck, A., Seurat, G., Stevens, B., Totems, J., Touzé-Peiffer, L., Vergez, G., Vial, J., Villiger, L., and Vogel, R.: EUREC[4]A observations from the SAFIRE ATR42 aircraft, Earth System Science Data, 14, 2021–2064, https://doi.org/10.5194/essd-14-2021-2022, 2022.

Bosser, P., Bock, O., Flamant, C., Bony, S., and Speich, S.: Integrated water vapour content retrievals from ship-borne GNSS receivers during EUREC[4]A, Earth System Science Data, 13, 1499–1517, https://doi.org/10.5194/essd-13-1499-2021, 2021.

Cadeddu, M., Turner, D., and Liljegren, J.: A Neural Network for Real-Time Retrievals of PWV and LWP From Arctic Millimeter-Wave Ground-Based Observations, IEEE Transactions on Geoscience and Remote Sensing, https://doi.org/10.1109/TGRS.2009.2013205, 2009.

Crewell, S. and Lohnert, U.: Accuracy of Boundary Layer Temperature Profiles Retrieved With Multifrequency Multiangle Microwave Radiometry, IEEE Transactions on Geoscience and Remote Sensing, 45, 2195–2201, https://doi.org/10.1109/TGRS.2006.888434, 2007.

Crewell, S. and Löhnert, U.: Accuracy of cloud liquid water path from ground-based microwave radiometry 2. Sensor accuracy and synergy, Radio Science, 38, https://doi.org/10.1029/2002RS002634, 2003.

Dufresne, J.-L. and Bony, S.: An Assessment of the Primary Sources of Spread of Global Warming Estimates from Coupled Atmosphere–Ocean Models, Journal of Climate, 21, 5135–5144, https://doi.org/10.1175/2008JCLI2239.1, 2008.

Ebell, K., Löhnert, U., Päschke, E., Orlandi, E., Schween, J. H., and Crewell, S.: A 1-D variational retrieval of temperature, humidity, and liquid cloud properties: Performance under idealized and real conditions, Journal of Geophysical Research: Atmospheres, 122, 1746–1766, https://doi.org/10.1002/2016JD025945, 2017.

Elsaesser, G. S., O'Dell, C. W., Lebsock, M. D., Bennartz, R., Greenwald, T. J., and Wentz, F. J.: The Multisensor Advanced Climatology of Liquid Water Path (MAC-LWP), Journal of Climate, 30, 10 193–10 210, https://doi.org/10.1175/JCLI-D-16-0902.1, 2017.

Foster, J., Bevis, M., and Raymond, W.: Precipitable water and the lognormal distribution, Journal of Geophysical Research: Atmospheres, 111, https://doi.org/10.1029/2005JD006731, 2006.

George, G., Stevens, B., Bony, S., Pincus, R., Fairall, C., Schulz, H., Kölling, T., Kalen, Q. T., Klingebiel, M., Konow, H., Lundry, A., Prange, M., and Radtke, J.: JOANNE: Joint dropsonde Observations of the Atmosphere in tropical North atlaNtic meso-scale Environments, Earth System Science Data, 13, 5253–5272, https://doi.org/10.5194/essd-13-5253-2021, 2021.

Hirsch, L.: Ka Band Cloud Radar Barbados Cloud Observatory, EUREC4A, AERIS [Dataset], https://doi.org/https://doi.org/10.25326/55, 2022.

Illingworth, A. J., Hogan, R. J., O'Connor, E. J., Bouniol, D., Brooks, M. E., Delanoé, J., Donovan, D. P., Eastment, J. D., Gaussiat, N., Goddard, J. W. F., Haeffelin, M., Baltink, H. K., Krasnov, O. A., Pelon, J., Piriou, J.-M., Protat, A., Russchenberg, H. W. J., Seifert, A., Tompkins, A. M., van Zadelhoff, G.-J., Vinit, F., Willén, U., Wilson, D. R., and Wrench, C. L.: Cloudnet: Continuous Evaluation of Cloud Profiles in Seven Operational Models Using Ground-Based Observations, Bulletin of the American Meteorological Society, 88, 883–898, https://doi.org/10.1175/BAMS-88-6-883, 2007.

Jacob, M.: Liquid water path and integrated water vapor over the tropical Atlantic during EUREC4A, AERIS [Dataset], https://doi.org/10.25326/247, 2021.

Jacob, M., Ament, F., Gutleben, M., Konow, H., Mech, M., Wirth, M., and Crewell, S.: Investigating the liquid water path over the tropical Atlantic with synergistic airborne measurements, Atmospheric Measurement Techniques, 12, 3237–3254, https://doi.org/10.5194/amt-12-3237-2019, 2019.

Jahangir, E., Libois, Q., Couvreux, F., Vié, B., and Saint-Martin, D.: Uncertainty of SW Cloud Radiative Effect in Atmospheric Models Due to the Parameterization of Liquid Cloud Optical Properties, Journal of Advances in Modeling Earth Systems, 13, e2021MS002742, https://doi.org/10.1029/2021MS002742, 2021.

Kalesse-Los, H., Röttenbacher, J., Schäfer, M., and Emmanouilidis, A.: Microwave Radiometer Measurements RV Meteor, EUREC4A, AERIS [Dataset], https://doi.org/doi.org/10.25326/77, 2020.

Kalesse-Los, H., Kötsche, A., Foth, A., Röttenbacher, J., Vogl, T., and Witthuhn, J.: The Virga-Sniffer – a new tool to identify precipitation evaporation using ground-based remote-sensing observations, Atmospheric Measurement Techniques, 16, 1683–1704, https://doi.org/10.5194/amt-16-1683-2023, 2023.

Karstens, U., Simmer, C., and Ruprecht, E.: Remote sensing of cloud liquid water, Meteorology and Atmospheric Physics, 54, 157–171, https://doi.org/10.1007/BF01030057, 1994.

Konow, H., Ewald, F., George, G., Jacob, M., Klingebiel, M., Kölling, T., Luebke, A. E., Mieslinger, T., Pörtge, V., Radtke, J., Schäfer, M., Schulz, H., Vogel, R., Wirth, M., Bony, S., Crewell, S., Ehrlich, A., Forster, L., Giez, A., Gödde, F., Groß, S., Gutleben, M., Hagen, M., Hirsch, L., Jansen, F., Lang, T., Mayer, B., Mech, M., Prange, M., Schnitt, S., Vial, J., Walbröl, A., Wendisch, M., Wolf, K., Zinner, T., Zöger, M., Ament, F., and Stevens, B.: EUREC^{4}A's *HALO*, Earth System Science Data, 13, 5545–5563, https://doi.org/10.5194/essd-13-5545-2021, 2021.

Küchler, N., Kneifel, S., Löhnert, U., Kollias, P., Czekala, H., and Rose, T.: A W-Band Radar–Radiometer System for Accurate and Continuous Monitoring of Clouds and Precipitation, Journal of Atmospheric and Oceanic Technology, 34, 2375–2392, https://doi.org/10.1175/JTECH-D-17-0019.1, 2017.

Löhnert, U. and Crewell, S.: Accuracy of cloud liquid water path from ground-based microwave radiometry 1. Dependency on cloud model statistics, Radio Science, 38, 8041, https://doi.org/10.1029/2002RS002654, 2003.

Löhnert, U. and Maier, O.: Operational profiling of temperature using ground-based microwave radiometry at Payerne: prospects and challenges, Atmospheric Measurement Techniques, 5, 1121–1134, https://doi.org/10.5194/amt-5-1121-2012, 2012.

Löhnert, U., Turner, D. D., and Crewell, S.: Ground-Based Temperature and Humidity Profiling Using Spectral Infrared and Microwave Observations. Part I: Simulated Retrieval Performance in Clear-Sky Conditions, Journal of Applied Meteorology and Climatology, 48, 1017–1032, https://doi.org/10.1175/2008JAMC2060.1, 2009.

Maschwitz, G., Löhnert, U., Crewell, S., Rose, T., and Turner, D. D.: Investigation of ground-based microwave radiometer calibration techniques at 530 hPa, Atmospheric Measurement Techniques, 6, 2641–2658, https://doi.org/10.5194/amt-6-2641-2013, 2013.

Mech, M., Orlandi, E., Crewell, S., Ament, F., Hirsch, L., Hagen, M., Peters, G., and Stevens, B.: HAMP – the microwave package on the High Altitude and LOng range research aircraft (HALO), Atmospheric Measurement Techniques, 7, 4539–4553, https://doi.org/10.5194/amt-7-4539-2014, 2014.

Mech, M., Maahn, M., Kneifel, S., Ori, D., Orlandi, E., Kollias, P., Schemann, V., and Crewell, S.: PAMTRA 1.0: the Passive and Active Microwave radiative TRAnsfer tool for simulating radiometer and radar measurements of the cloudy atmosphere, Geoscientific Model Development, 13, 4229–4251, https://doi.org/10.5194/gmd-13-4229-2020, 2020.

Mieslinger, T., Stevens, B., Kölling, T., Brath, M., Wirth, M., and Buehler, S. A.: Optically thin clouds in the trades, Atmospheric Chemistry and Physics, 22, 6879–6898, https://doi.org/10.5194/acp-22-6879-2022, 2022.

Nuijens, L., Serikov, I., Hirsch, L., Lonitz, K., and Stevens, B.: The distribution and variability of low-level cloud in the North Atlantic trades, Quarterly Journal of the Royal Meteorological Society, 140, 2364–2374, https://doi.org/10.1002/qj.2307, 2014.

Pincus, R., Fairall, C. W., Bailey, A., Chen, H., Chuang, P. Y., de Boer, G., Feingold, G., Henze, D., Kalen, Q. T., Kazil, J., Leandro, M., Lundry, A., Moran, K., Naeher, D. A., Noone, D., Patel, A. J., Pezoa, S., PopStefanija, I., Thompson, E. J., Warnecke, J., and Zuidema, P.: Observations from the NOAA P-3 aircraft during ATOMIC, Earth System Science Data, 13, 3281–3296, https://doi.org/10.5194/essd-13-3281-2021, 2021.

Rose, T., Crewell, S., Löhnert, U., and Simmer, C.: A network suitable microwave radiometer for operational monitoring of the cloudy atmosphere, Atmospheric Research, 75, 183–200, https://doi.org/10.1016/j.atmosres.2004.12.005, 2005.

Schnitt, S., Orlandi, E., Mech, M., Ehrlich, A., and Crewell, S.: Characterization of Water Vapor and Clouds During the Next-Generation Aircraft Remote Sensing for Validation (NARVAL) South Studies, IEEE Journal of Selected Topics in Applied Earth Observations and Remote Sensing, 10, 3114–3124, https://doi.org/10.1109/JSTARS.2017.2687943, 2017.

Schnitt, S., Foth, A., Kalesse-Los, H., Mech, M., and Acquistapace, C.: Ground- and ship-based microwave radiometer measurements during EUREC4A, AERIS [Dataset], https://doi.org/10.25326/454, 2023.

Schulz, H., Eastman, R., and Stevens, B.: Characterization and Evolution of Organized Shallow Convection in the Downstream North Atlantic Trades, Journal of Geophysical Research: Atmospheres, 126, e2021JD034 575, https://doi.org/10.1029/2021JD034575, 2021.

Steinke, S., Eikenberg, S., Löhnert, U., Dick, G., Klocke, D., Di Girolamo, P., and Crewell, S.: Assessment of small-scale integrated water vapour variability during HOPE, Atmospheric Chemistry and Physics, 15, 2675–2692, https://doi.org/10.5194/acp-15-2675-2015, 2015.

Stephan, C. C., Schnitt, S., Schulz, H., Bellenger, H., de Szoeke, S. P., Acquistapace, C., Baier, K., Dauhut, T., Laxenaire, R., Morfa-Avalos, Y., Person, R., Quiñones Meléndez, E., Bagheri, G., Böck, T., Daley, A., Güttler, J., Helfer, K. C., Los, S. A., Neuberger, A., Röttenbacher, J., Raeke, A., Ringel, M., Ritschel, M., Sadoulet, P., Schirmacher, I., Stolla, M. K., Wright, E., Charpentier, B., Doerenbecher, A., Wilson, R., Jansen, F., Kinne, S., Reverdin, G., Speich, S., Bony, S., and Stevens, B.: Ship- and island-based atmospheric soundings from the 2020 EUREC4A field campaign, Earth System Science Data, 13, 491–514, https://doi.org/https://doi.org/10.5194/essd-13-491-2021, 2021.

Stevens, B. and Kluft, L.: A Colorful look at Climate Sensitivity, EGUsphere, pp. 1–24, https://doi.org/10.5194/egusphere-2022-1460, 2023.

Stevens, B., Farrell, D., Hirsch, L., Jansen, F., Nuijens, L., Serikov, I., Brügmann, B., Forde, M., Linne, H., Lonitz, K., and Prospero, J. M.: The Barbados Cloud Observatory: Anchoring Investigations of Clouds and Circulation on the Edge of the ITCZ, Bulletin of the American Meteorological Society, 97, 787–801, https://doi.org/10.1175/BAMS-D-14-00247.1, 2016.

630 Stevens, B., Ament, F., Bony, S., Crewell, S., Ewald, F., Gross, S., Hansen, A., Hirsch, L., Jacob, M., Kölling, T., Konow, H., Mayer, B., Wendisch, M., Wirth, M., Wolf, K., Bakan, S., Bauer-Pfundstein, M., Brueck, M., Delanoë, J., Ehrlich, A., Farrell, D., Forde, M., Gödde, F., Grob, H., Hagen, M., Jäkel, E., Jansen, F., Klepp, C., Klingebiel, M., Mech, M., Peters, G., Rapp, M., Wing, A. A., and Zinner, T.: A High-Altitude Long-Range Aircraft Configured as a Cloud Observatory: The NARVAL Expeditions, Bulletin of the American Meteorological Society, 100, 1061–1077, https://doi.org/10.1175/BAMS-D-18-0198.1, 2019.

635 Stevens, B., Bony, S., Farrell, D., Ament, F., Blyth, A., Fairall, C., Karstensen, J., Quinn, P. K., Speich, S., Acquistapace, C., Aemisegger, F., Albright, A. L., Bellenger, H., Bodenschatz, E., Caesar, K.-A., Chewitt-Lucas, R., de Boer, G., Delanoë, J., Denby, L., Ewald, F., Fildier, B., Forde, M., George, G., Gross, S., Hagen, M., Hausold, A., Heywood, K. J., Hirsch, L., Jacob, M., Jansen, F., Kinne, S., Klocke, D., Kölling, T., Konow, H., Lothon, M., Mohr, W., Naumann, A. K., Nuijens, L., Olivier, L., Pincus, R., Pöhlker, M., Reverdin, G., Roberts, G., Schnitt, S., Schulz, H., Siebesma, A. P., Stephan, C. C., Sullivan, P., Touzé-Peiffer, L., Vial, J., Vogel, R., Zuidema, P., Alexander, 640 N., Alves, L., Arixi, S., Asmath, H., Bagheri, G., Baier, K., Bailey, A., Baranowski, D., Baron, A., Barrau, S., Barrett, P. A., Batier, F., Behrendt, A., Bendinger, A., Beucher, F., Bigorre, S., Blades, E., Blossey, P., Bock, O., Böing, S., Bosser, P., Bourras, D., Bouruet-Aubertot, P., Bower, K., Branellec, P., Branger, H., Brennek, M., Brewer, A., Brilouet, P.-E., Brügmann, B., Buehler, S. A., Burke, E., Burton, R., Calmer, R., Canonici, J.-C., Carton, X., Cato Jr., G., Charles, J. A., Chazette, P., Chen, Y., Chilinski, M. T., Choularton, T., Chuang, P., Clarke, S., Coe, H., Cornet, C., Coutris, P., Couvreux, F., Crewell, S., Cronin, T., Cui, Z., Cuypers, Y., Daley, A., Damerell, 645 G. M., Dauhut, T., Deneke, H., Desbios, J.-P., Dörner, S., Donner, S., Douet, V., Drushka, K., Dütsch, M., Ehrlich, A., Emanuel, K., Emmanouilidis, A., Etienne, J.-C., Etienne-Leblanc, S., Faure, G., Feingold, G., Ferrero, L., Fix, A., Flamant, C., Flatau, P. J., Foltz, G. R., Forster, L., Furtuna, I., Gadian, A., Galewsky, J., Gallagher, M., Gallimore, P., Gaston, C., Gentemann, C., Geyskens, N., Giez, A., Gollop, J., Gouirand, I., Gourbeyre, C., de Graaf, D., de Groot, G. E., Grosz, R., Güttler, J., Gutleben, M., Hall, K., Harris, G., Helfer, K. C., Henze, D., Herbert, C., Holanda, B., Ibanez-Landeta, A., Intrieri, J., Iyer, S., Julien, F., Kalesse, H., Kazil, J., Kellman, A., Kidane, 650 A. T., Kirchner, U., Klingebiel, M., Körner, M., Kremper, L. A., Kretzschmar, J., Krüger, O., Kumala, W., Kurz, A., L'Hégaret, P., Labaste, M., Lachlan-Cope, T., Laing, A., Landschützer, P., Lang, T., Lange, D., Lange, I., Laplace, C., Lavik, G., Laxenaire, R., Le Bihan, C., Leandro, M., Lefevre, N., Lena, M., Lenschow, D., Li, Q., Lloyd, G., Los, S., Losi, N., Lovell, O., Luneau, C., Makuch, P., Malinowski, S., Manta, G., Marinou, E., Marsden, N., Masson, S., Maury, N., Mayer, B., Mayers-Als, M., Mazel, C., McGeary, W., McWilliams, J. C., Mech, M., Mehlmann, M., Meroni, A. N., Mieslinger, T., Minikin, A., Minnett, P., Möller, G., Morfa Avalos, Y., Muller, C., Musat, I., 655 Napoli, A., Neuberger, A., Noisel, C., Noone, D., Nordsiek, F., Nowak, J. L., Oswald, L., Parker, D. J., Peck, C., Person, R., Philippi, M., Plueddemann, A., Pöhlker, C., Pörtge, V., Pöschl, U., Pologne, L., Posyniak, M., Prange, M., Quiñones Meléndez, E., Radtke, J., Ramage, K., Reimann, J., Renault, L., Reus, K., Reyes, A., Ribbe, J., Ringel, M., Ritschel, M., Rocha, C. B., Rochetin, N., Röttenbacher, J., Rollo, C., Royer, H., Sadoulet, P., Saffin, L., Sandiford, S., Sandu, I., Schäfer, M., Schemann, V., Schirmacher, I., Schlenczek, O., Schmidt, J., Schröder, M., Schwarzenboeck, A., Sealy, A., Senff, C. J., Serikov, I., Shohan, S., Siddle, E., Smirnov, A., Späth, F., Spooner, B., Stolla, 660 M. K., Szkółka, W., de Szoeke, S. P., Tarot, S., Tetoni, E., Thompson, E., Thomson, J., Tomassini, L., Totems, J., Ubele, A. A., Villiger, L., von Arx, J., Wagner, T., Walther, A., Webber, B., Wendisch, M., Whitehall, S., Wiltshire, A., Wing, A. A., Wirth, M., Wiskandt, J., Wolf, K., Worbes, L., Wright, E., Wulfmeyer, V., Young, S., Zhang, C., Zhang, D., Ziemen, F., Zinner, T., and Zöger, M.: EUREC[4]A, Earth System Science Data, 13, 4067–4119, https://doi.org/10.5194/essd-13-4067-2021, 2021.

Stokes, G. M. and Schwartz, S. E.: The Atmospheric Radiation Measurement (ARM) Program: Programmatic Background and Design

665   of the Cloud and Radiation Test Bed, Bulletin of the American Meteorological Society, 75, 1201–1222, https://doi.org/10.1175/1520-0477(1994)075<1201:TARMPP>2.0.CO;2, 1994.

Ulaby, F. T.: Microwave radar and radiometric remote sensing, The University of Michigan Press, Ann Arbor, 2014.

van Meijgaard, E. and Crewell, S.: Comparison of model predicted liquid water path with ground-based measurements during CLIWA-NET, Atmospheric Research, 75, 201–226, https://doi.org/10.1016/j.atmosres.2004.12.006, 2005.

670   Vial, J., Dufresne, J.-L., and Bony, S.: On the interpretation of inter-model spread in CMIP5 climate sensitivity estimates, Climate Dynamics, 41, 3339–3362, https://doi.org/10.1007/s00382-013-1725-9, 2013.

Walbröl, A., Crewell, S., Engelmann, R., Orlandi, E., Griesche, H., Radenz, M., Hofer, J., Althausen, D., Maturilli, M., and Ebell, K.: Atmospheric temperature, water vapour and liquid water path from two microwave radiometers during MOSAiC, Scientific Data, 9, 534, https://doi.org/10.1038/s41597-022-01504-1, 2022.

675   Westwater, E. R.: The accuracy of water vapor and cloud liquid determination by dual-frequency ground-based microwave radiometry, Radio Science, 13, 677–685, https://doi.org/10.1029/RS013i004p00677, 1978.

Zelinka, M. D., Myers, T. A., McCoy, D. T., Po-Chedley, S., Caldwell, P. M., Ceppi, P., Klein, S. A., and Taylor, K. E.: Causes of Higher Climate Sensitivity in CMIP6 Models, Geophysical Research Letters, 47, e2019GL085 782, https://doi.org/10.1029/2019GL085782, 2020.